Earth and Planetary Science Letters 444 (2016) 56–63

Contents lists available at ScienceDirect

Earth and Planetary Science Letters

www.elsevier.com/locate/epsl

Physical processes in Subglacial Lake Whillans, West Antarctica: Inferences from sediment cores

T.O. Hodson [a,*], R.D. Powell [a], S.A. Brachfeld [b], S. Tulaczyk [c], R.P. Scherer [a], WISSARD Science Team [1]

[a] Department of Geological & Environmental Geosciences, Northern Illinois University, DeKalb, IL, USA
[b] Department of Earth and Environmental Studies, Montclair State University, Montclair, NJ, USA
[c] Department of Earth and Planetary Sciences, University of California, Santa Cruz, CA, USA

ARTICLE INFO

Article history:
Received 8 January 2016
Received in revised form 15 March 2016
Accepted 18 March 2016
Available online 6 April 2016
Editor: P. Shearer

Keywords:
subglacial lakes
glaciology
ice streams
Antarctica
subglacial access

ABSTRACT

The hydrologic system beneath the Antarctic Ice Sheet is thought to influence both the dynamics and distribution of fast flowing ice streams, which discharge most of the ice lost by the ice sheet. Despite considerable interest in understanding this subglacial network and its affect on ice flow, *in situ* observations from the ice sheet bed are exceedingly rare. Here we describe the first sediment cores recovered from an active subglacial lake. The lake, known as Subglacial Lake Whillans, is part of a broader, dynamic hydrologic network beneath the Whillans Ice Stream in West Antarctica. Even though "floods" pass through the lake, the lake floor shows no evidence of erosion or deposition by flowing water. By inference, these floods must have insufficient energy to erode or transport significant volumes of sediment coarser than silt. Consequently, water flow beneath the region is probably incapable of incising continuous channels into the bed and instead follows preexisting subglacial topography and surface slope. Sediment on the lake floor consists of till deposited during intermittent grounding of the ice stream following flood events. The fabrics within the till are weaker than those thought to develop in thick deforming beds suggesting subglacial sediment fluxes across the ice plain are currently low and unlikely to have a large stabilizing effect on the ice stream's grounding zone.

1. Introduction

Roughly 400 subglacial lakes are currently thought to exist beneath the Antarctic Ice Sheet where its base is at the pressure melting point (Wright and Siegert, 2012). These lakes have generated scientific interest for their potential to harbor unique microbial ecosystems (Christner et al., 2014; Priscu et al., 1999), influence ice dynamics (Bell et al., 2007; Stearns et al., 2008), and preserve paleoclimate or paleoenvironmental records in their sediments (Bentley et al., 2011). Large deep lakes in the interior, such as Subglacial Lake Vostok, may have existed continuously through the late Cenozoic and potentially contain sedimentary records of the early evolution of the East Antarctic Ice Sheet (Siegert et al., 2001). Other shallower lakes beneath fast flowing ice streams near the ice sheet margin might contain sedimentary records of the dynamic subglacial hydrologic system, which is thought to regulate ice streaming (Anandakrishnan and Alley, 1997). As ice streams discharge 90% of the ice lost from the Antarctic, their dynamics determine the rate at which the ice sheet can affect global sea level (Bamber et al., 2009).

Ice streams occur in zones of low basal drag, where a combination of soft sediments and low effective pressures, the difference between ice overburden pressure and water pressure, act to lubricate the ice sheet bed. As ice stream driving stresses are low, due to their low surface slopes, even small changes within the subglacial hydrologic system can potentially have large effects on basal drag and ice flow (Anandakrishnan and Alley, 1997).

Ice streams are also sensitive to processes at their grounding zones, where they transition to floating ice shelves. When ice streams occur over reverse sloping beds, any retreat places the grounding zone in deeper water where the ice thickness is greater. As the ice flux across the grounding zone increases nonlinearly with ice thickness, this creates a potential for runaway retreat with increasing rates of ice loss (Schoof, 2007; Weertman, 1974). Such a

* Corresponding author at: Department of Geology and Environmental Geosciences, Northern Illinois University, Davis Hall 312, Normal Rd., DeKalb, IL 60115, USA. Tel.: +1 815 753 1943.
E-mail address: tohodson@gmail.com (T.O. Hodson).
[1] Full list at http://www.wissard.org/about/wissard-personnel.

http://dx.doi.org/10.1016/j.epsl.2016.03.036
0012-821X/

retreat could be triggered by increased melting across the bottom of the ice shelf, thinning the ice and reducing its buttressing effect, or by focused melting at the grounding zone (Rignot and Jacobs, 2002). However, a number of internal mechanisms may counter this instability, including sediment deposition at the grounding zone, which reduces water depth, preventing the ice from going afloat as it thins, and increases the frictional drag from the bed, helping to buttress the ice sheet margin (Alley et al., 2007; Anandakrishnan et al., 2007). Ice stream dynamics therefore reflect a broad range of processes that integrate glaciology, hydrology, geology, and oceanography (Anandakrishnan et al., 1998; Bindschadler et al., 2003; Clarke, 2005), specifics of which are not well understood, due to the difficulty of accessing and sampling the ice sheet bed. Nevertheless, defining and predicting ice sheet stability requires that we constrain the dynamics of these systems (Joughin et al., 2014; Rignot et al., 2014).

We describe the first sediments recovered from an active Antarctic subglacial lake. The lake, known as Subglacial Lake Whillans (SLW), sits beneath the 800 m thick Whillans Ice Plain (WIP), the lowermost section of the Whillans Ice Stream (WIS) before it goes afloat and flows into the Ross Ice Shelf (Fig. 1a). SLW and other active lakes underlie at least ~10% of this region and were first identified from the short-term fluctuations in the overlying ice surface elevation driven by cyclic draining and filling of the lake waters (Fricker et al., 2007).

From the beginning of satellite altimetric observation in 2004 to our sampling of the lake, SLW had undergone two such fill-and-drain cycles, each lasting approximately two years and separated by quiescent lowstands of more variable duration. When the lake drains, roughly 0.15 km^3 of water discharges over a six-month period, lowering the ice elevation above the lake by up to 5 m (Christianson et al., 2012; Fricker et al., 2007). Prior to our sampling in January 2013, the last drainage occurred in 2009, during which ice surface elevations above the lake dropped to ~0.8 m above their lowest observed level (Fig. 1b). Between that drainage and our accessing the lake, the ice surface gradually rose another 0.42 m, due to either the lake filling or the ice stream thickening (Pritchard et al., 2012; Siegfried et al., 2014).

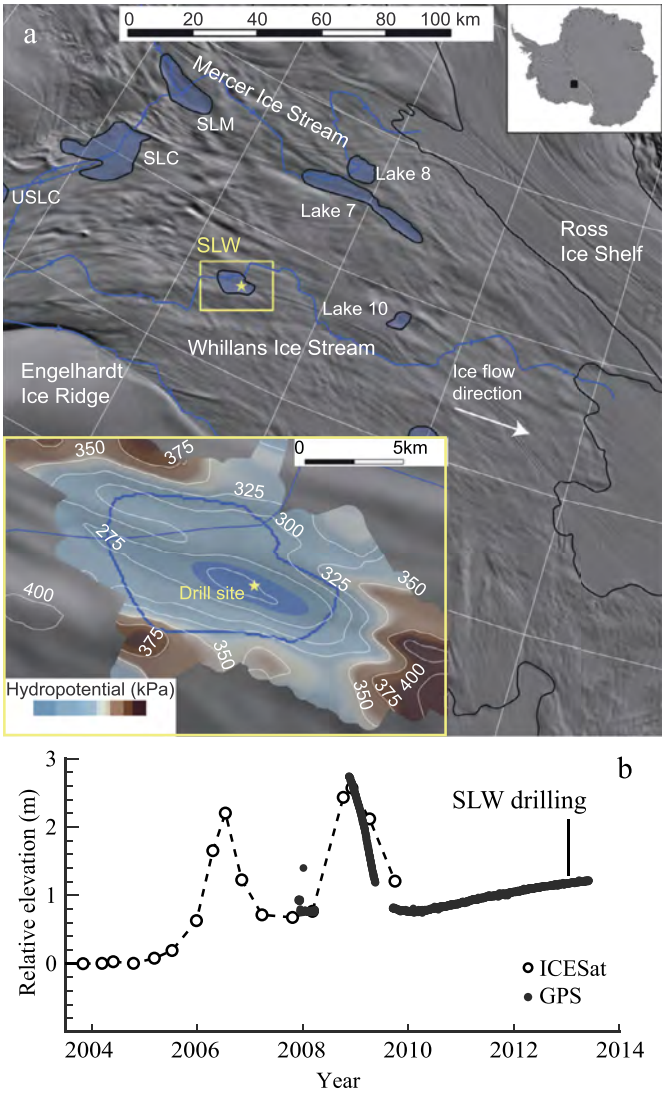

Fig. 1. a) Location of the WIS and SLW [from Christner et al., 2014 and references therein]. The maximum extent of SLW and other subglacial lakes in blue; predicted subglacial water flowpaths through SLW and other subglacial lakes are represented by blue lines with arrows; the black line denotes the ice-sheet grounding line at the start of the Ross Ice Shelf. Inset shows details of SLW with both maximum (solid blue line) and minimum lake extent (shaded blue area), hydropotential contours (white isolines; 25 kPa interval), and drill site (yellow star; 84.240°S 153.694°W). Background imagery is MODIS MOA30. **b)** Relative change in average lake surface elevation between 2004 and 2014 (Siegfried et al., 2014). (For interpretation of the references to color in this figure legend, the reader is referred to the web version of this article.)

2. Methods

2.1. Coring operations

Three coring devices were deployed into SLW: a gravity multicorer with three 60 mm diameter core barrels designed to recover the soft upper-most sediment and sediment-water interface; a borehole piston corer with a 58 mm diameter core barrel; and a percussion corer with a 10 cm diameter core barrel (Hodgson et al., 2016). Due to a malfunction, percussion-coring was ceased after 10 min (approx. 10 blows of the weight). All sediment cores were collected within a 40-h window, during which time the borehole moved roughly 1 m downstream (Tulaczyk et al., 2014). In total, an 80 cm long piston core, a 40 cm long percussion core, and six multicores between 20–40 cm long were recovered. Once the sediment cores reached the surface, they were set vertically for at least two days to allow them to outgas and settle before being laid horizontally for packing and refrigerated (4 °C) shipping and long-term storage.

2.2. Whole core measurements

Sediment cores were split, logged, and sampled at the Hartshorne Quaternary Lab at University of Massachusetts, Amherst. High-resolution line-scan imagery, gamma ray attenuation bulk density and magnetic susceptibility were logged for both whole and split cores using a Geotek multi-sensor core logger. High-resolution ED-XRF spectra were logged on the split cores at a 0.3 mm interval using an ITRAX XRF core scanner, which irradiated the sample with a beam generated from a 3 kW Mo target run at 45 kV and 30 mA over a 15 s exposure time. In addition to line-scan radiographs generated by the ITRAX, high-resolution core radiographs of the split cores were taken using a Torrex 120-D radiograph at Antarctic Marine Geology Research Facility, Florida State University.

2.3. Moisture content and particle size

Sediment moisture content was measured at ~2–5 cm intervals by measuring the weight lost after oven drying the sample for 24 h at 110 °C. Initial wet sample weights ranged between 20 and 50 g. After oven drying, the samples were disaggregated and their particle sizes were analyzed using sieve and pipette methods. As variable clast content in diamicton samples influence measure-

ments of moisture content, the weight of the gravel fraction was subtracted from the bulk weight in determining moisture content. Additional particle size analysis using laser diffractometry was performed at ~10 cm intervals. Approximately 5 g of sediment was gently disaggregated and dry-sieved to remove gravel (>2 mm). An aliquot of the sieved sample was then transferred into a glass bottle with 0.5 ml 5% sodium hexametaphosphate solution and 30 ml deionized water. Samples were then shaken for 8 h prior to analysis on a Malvern Mastersizer 3000.

2.4. Magnetic fabric and magnetic granulometry

2 cm wide oriented paleomagnetic cubes were collected every 4–10 cm along each core for analysis of anisotropy of magnetic susceptibility (AMS) and natural remnant magnetization (NRM). Samples were taken from the center of the cores to avoid disturbance that typically occurs along the outside edge of the core. Unoriented samples were collected at each depth for magnetic granulometry. Stepwise alternating field (AF) demagnetization and measurement of the NRM was performed using a D-tech D-2000 alternating field demagnetizer and AGICO JR-6 spinner magnetometer. Samples were subjected to peak fields of 0 to 80 mT in 5–10 mT increments. AMS measurements were made using an AGICO KLY-4 Kappabridge at Montclair State University. The magnetic susceptibility of each cube was measured in 15 orientations, yielding a second-rank susceptibility tensor. The eigenvalues of this tensor are the three principal magnetic susceptibilities, k_{max}, k_{int}, and k_{min}, which represent the lengths of the long, intermediate, and short axes of a susceptibility ellipsoid. The orientation of each axis (eigenvector) is given by its inclination (I) and declination (D). Two parameters representing the shape of the AMS ellipsoid are the lineation parameter ($L = k_{max}/k_{min}$), and foliation ($F = k_{int}/k_{min}$). $L < F$ indicates an oblate ellipsoid. $L > F$ indicates a prolate ellipsoid.

AMS fabrics in sediment can arise from the preferential alignment of ferromagnetic and paramagnetic grains during deposition or post-depositional processes, or by coring-induced disturbance. Disturbed portions of the sediment cores were identified by horizontal values of I_{min} and near-vertical values of I_{max} indicating core stretching (Thouveny et al., 2000) or by anomalously high foliation, which can indicate coring-induced compaction.

Magnetic domain state and magnetic mineralogy were determined from hysteresis parameters, thermomagnetic curves, and scanning electron microscopy and energy-dispersive X-ray spectrometry. Hysteresis parameters were measured on bulk sediment using a Princeton Measurements Corp. Vibrating Sample Magnetometer (VSM). Thermomagnetic curves were measured on bulk sediment on an AGICO KLY4 Kappabridge from 20 to 700 °C in a flowing argon gas atmosphere. Polished grain mounts were analyzed on a Hitachi S3400N scanning electron microscope equipped with a Bruker X-flash X-ray microanalysis system.

2.5. Sediment micromorphology

Sedimentary microfabrics result from the reorientation of sand, silt, and clay grains in response to a deforming stress. Like AMS, microfabrics can help distinguish depositional processes in macroscopically structureless tills. Microfabrics are also susceptible to even small strains (Hiemstra and Rijsdijk, 2003) giving them the potential record disturbance from coring or degassing that may impact NRM and AMS fabrics.

Three 75 × 35 mm sections were extracted from the piston core from shallow (15–22.5 cm), intermediate (34–42 cm), and deep (67–74 cm) intervals and one from the percussion core (23.5–31 cm) for micromorphological analysis. The sections were freeze-dried and impregnated with epoxy prior to being cut into thin sections. Each thin section was oriented with respect to vertical but their orientation relative to ice flow is unknown. Microfabrics in the sediments were described following standard terminology used in the glacial literature (i.e., van der Meer, 1993; van der Meer and Menzies, 2011).

2.6. Sediment lithology

Thin sections made from grain mounts were prepared from size-sorted grains from each phi size fraction between 500 to 2000 µm. Approximately 300 grains in each sample were identified under a petrographic microscope and tallied while making systematic transects across the thin section. The point counts from each size fraction were then aggregated over the 500–2000 µm range, with each fraction weighted according to the particle size distribution.

3. Results

Sediment cores recovered through the 800 m deep borehole into SLW contain dark gray muddy diamicton, consisting of 8% granules and pebbles, 33% sand, 26% silt and 33% clay, similar to basal sediment sampled ~200 km upstream on the Whillans Ice Stream at a site known as Upstream B (UpB; Tulaczyk et al., 1998). The composition of the sand fraction is indistinguishable from UpB and similar to other samples from the Siple Coast and Eastern Ross Sea Region (Licht et al., 2005). Common lithologies include hydrothermally altered felsic intrusives and metasedimentary schists and phyllites. Sedimentary and extrusive rock fragments each constitute ≤1% (Appendix A). With the exception of thin (1–2 mm diameter) degassing tubules, the sediment appears structureless. X-radiographs of the cores show variable clast content with depth but otherwise no discernable stratification or grading (Fig. 2a). High-resolution scans of element chemistry and bulk magnetic susceptibility show negligible stratigraphic variability in chemical and physical properties suggesting the sediment is very homogeneous over the sampling depth (~0.8 m). Log density also shows no trend despite a logarithmic decrease in moisture content with depth. This difference likely reflects the presence of air filled voids, formed by outgassing as the cores equilibrated to conditions at the surface. Moisture content, which is unaffected by degassing (Tulaczyk et al., 2001a), is 35% at the sediment-lake water interface. Assuming a compressibility similar to the till upstream (Tulaczyk et al., 2000), this high moisture content implies *in situ* effective stresses during deposition were low (≤1 kPa), similar to the environment inferred to be beneath much of the surrounding ice plain. Sedimentary microfabrics and microstructures within the cores are weakly developed and indicate ductile deformation consistent with shear under low basal effective pressure (e.g., Khatwa and Tulaczyk, 2001; Cowan et al., 2014). Fabric disturbance due to degassing is negligible; however, sections of the cores contain stronger microfabrics associated with coring disturbance that have overprinted the natural fabrics (Appendix B).

The magnetic mineral assemblage in the piston core and percussion core consists of magnetite and ilmenite, possibly with nano-scale hematite intergrowths (Appendix C). However, ilmenite is antiferromagnetic and does not contribute substantially to NRM or AMS signals. Magnetite ranges in size from fine pseudo-single-domain (PSD) to multidomain size, determined from the median destructive field of the NRM (35–40 mT) and from hysteresis loops that are dominated by the multidomain fraction (Appendix C). The magnetic mineral assemblage is uniform throughout PC1 and PEC, consistent with relatively constant Fe/Ti ratios determined from XRF measurements (Fig. 3).

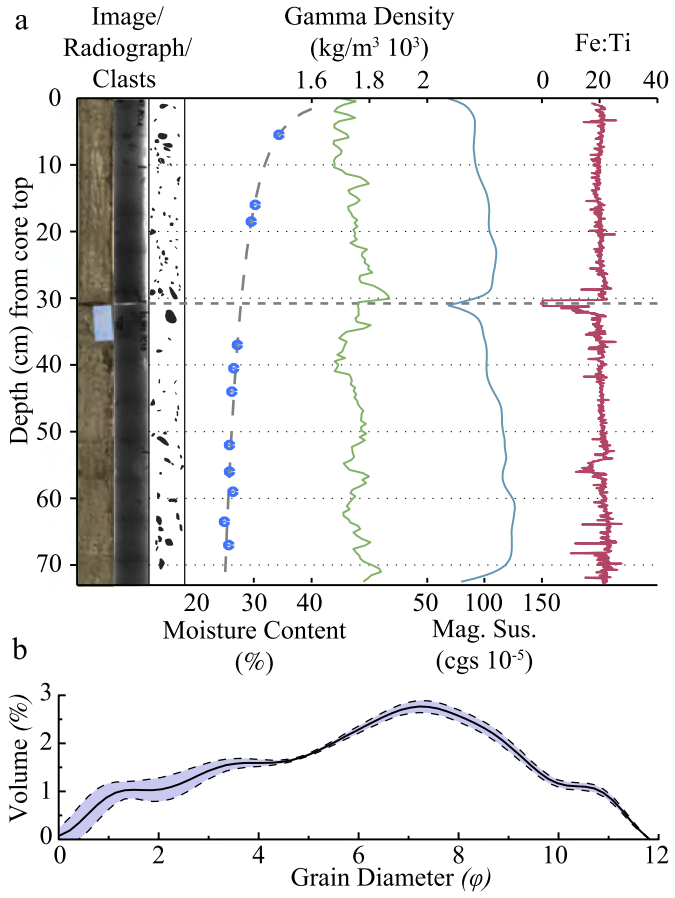

Fig. 2. a) Right to left: Geotek line-scan images of piston core (SLW1-PC1), core radiograph, digitized clasts, moisture content, Geotek wet bulk density, and ITRAX Fe:Ti. **b)** Particle size distribution of till matrix, measured by laser diffraction. The mean and 2-sigma distributions are shown by the solid line and shaded region, respectively.

Magnetic fabrics in the cores can be visualized on lower hemisphere, equal-area stereonets, where principal axes of the susceptibility ellipsoid are plotted according to their inclination (analogous to plunge on a stereonet) and declination (analogous to trend). Points that form a tight cluster indicate parallel axes, whereas points that form a great circle represent axes within a common plane. In the piston core, k_{min} axes (red circles) orient vertically, whereas k_{max} axes preferentially orient along a shallow-dipping plane (Fig. 3b). Although partially masked by coring disturbance, the percussion core displays a similar fabric (Appendix B). AMS fabrics in sediment affected only by axial loading, such as coring-induced compaction or natural consolidation, have no preferential azimuthal alignment of k_{int} or k_{max} (Tarling and Hrouda, 1993) indicating the SLW sediment has experienced some degree of horizontal shear.

Natural Remnant Magnetization (NRM) inclinations in the upper 10 cm of the piston core vary around −80°, consistent with modern International Geomagnetic Reference Field (IGRF) inclinations at the site. Below this depth, inclinations shallow to between −40° and −50°. These deeper samples deviate significantly from the modern paleomagnetic inclination and the geocentric axial dipole value for the site latitude, indicating post-depositional strain, either from consolidation or shear. Samples from the percussion core were uniformly poor recorders of NRM, consistent with coring disturbance inferred from micro- and AMS fabric.

4. Discussion

The access borehole was located over the deepest portion of SLW, which was ∼2 m deep in January 2013 (Tulaczyk et al., 2014). At the same time, the average ice elevation above the lake was ∼1 m higher than the lowest known level in 2004. We infer that the ice stream was grounded over most of the lake bed in 2004, although a small remnant volume of water may have been present at the drill site.

Structureless diamicton, such as that comprising the lake cores, can form from a number of processes including: rainout through lake waters of debris melted out from basal ice, subaqueous debris flows, or subglacial deformation during periods of grounding (Benn and Evans, 2014; Munro-Stasiuk, 2003). The sheared fabrics within the sediment argue against a rainout origin, and although similar fabrics develop in debris flows, the low gradient and relief of the lake basin makes this mode of deposition highly unlikely (Horgan et al., 2012).

Based on ring-shear experiments on tills, weak fabrics such as those in the SLW sediments indicate low strains. Conversely, under moderate to high strains the maximum susceptibility axes quickly cluster in the shear direction (Hooyer et al., 2008). Iverson et al. (2008) argue that highly clustered, high-strain, fabrics in tills are proof of a thick deforming bed, whereas weaker fabrics are more likely to occur under a more variable strain regime, such as in a thin deforming layer being plowed by protrusions on the ice bed.

Geomagnetic field recording by the surficial sediment does not necessarily conflict with the shear deformation implied by the AMS data. NRM fabrics can reorient to the ambient geomagnetic field under extremely low effective pressure, where the sediment–water mixture approaches its liquid limit. Thus, the same conditions that facilitate ice streaming may also be responsible for preserving NRM fabrics in some tills (Eyles et al., 1987; Gravenor et al., 1973; Stupavsky et al., 1974). NRM 'lock-in' depths of two decimeters up to several decimeters are typical for normally consolidated sediments (Snowball et al., 2013; Stoner et al., 2013). The addition of an ice overburden would increase consolidation, reducing the 'lock-in' depth; however, given the low effective pressure beneath the ice plain this effect should be small. Based on NRM inclinations in the piston core, 'lock-in' likely occurred at ∼10 cm below the sediment–water interface. That inclinations shallow but remain relatively stable below this indicate strains at these depths were low, consistent with the AMS results. Therefore, slip at the ice bed or deformation in the uppermost 10 cm of sediment must accommodate the high strains associated with ice stream flow.

Assuming the environment beneath the ice plain is similar to that in the lake basin during grounding events, a shallow deforming bed of the style suggested by the magnetic fabrics would transport <40 $m^3\,m^{-1}\,yr^{-1}$ of till, similar to fluxes estimated much further upstream (Tulaczyk et al., 2001b). To arrive at this flux estimate we also assume an ice bed velocity of 350 m/yr and plug flow through a <10 cm thick deforming horizon. In addition, a portion of the ice motion may be accommodated by basal slip, and strain rate typically decreases with depth across the shear zone (e.g., Hooyer et al., 2008). Thus, the actual till flux may be an order of magnitude lower than our upper estimate. Sediment transported subglacially across the ice plain ultimately accumulates at the grounding zone in the form of a grounding-zone wedge, which can potentially help to stabilize the grounding zone position (Alley et al., 2007). As Antarctic grounding-zone wedges are typically 10–20 km long (Dowdeswell and Fugelli, 2012), this till flux could accumulate a wedge at a rate of <4 mm/yr. Although this accumulation could mitigate the effects of current rates of sea level rise, it might not keep pace with some projections of the late 21st century (IPCC, 2014), and it is orders of magnitude slower than typical

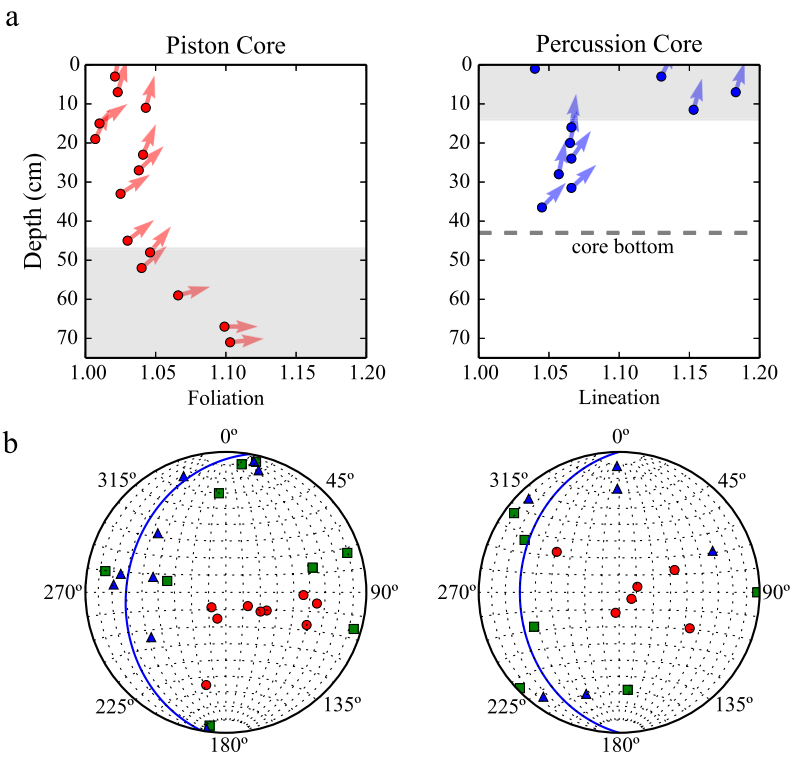

Fig. 3. AMS fabric in the piston core (left column) and percussion core (right column). **a)** Plots showing the variation in lineation ($L = k_{max}/k_{min}$) and foliation ($F = k_{int}/k_{min}$) versus depth in the piston and percussion cores respectively. Vectors represent the magnitude and inclination of the k_{min} principle susceptibility axis. **b)** Maximum (squares), intermediate (triangles), and minimum (circles) principal susceptibilities with disturbed sections omitted to highlight the natural fabric. k_{max} orientations trend towards a shallow plane depicted by the blue line. As the cores are not azimuthally oriented, the three principal susceptibility axes have been rotated by a constant so that the k_{min} axes plunge eastward or 'down-glacier', consistent with experimental observations from sheared diamict (Hooyer et al., 2008). (For interpretation of the references to color in this figure legend, the reader is referred to the web version of this article.)

melting rates driven by ocean thermal forcing (Rignot and Jacobs, 2002).

Despite SLW's history of filling and draining, sediment at and below the modern lakebed shows no evidence of sorting or scour that would indicate a high-velocity water flow. From the empirical Hjulstrom curve for a 1 m-deep flow, mean current velocities in the lake water column likely remain below 20 cm s^{-1} during draining cycles, which is consistent with water fluxes implied by ICESat altimetry (0.15 km^3 over 6 months; Fricker et al., 2007), if the flow occurs over the width of the lake. Thus, even though water flows through the subglacial drainage network in "floods" (Fricker and Scambos, 2009), the water has insufficient energy to erode or transport significant volumes of sediment coarser than silt. The dominance of till combined with the lack of stratified sediment or lags on the lake floor suggest sediment fluxes through the hydrologic network upstream and downstream of the lake are low, even relative to the low till flux. By inference, meltwater flow across the central WIP is generally incapable of incising continuous canals into bed and instead occurs through a more distributed system, maintained, at least in part, by hydrologic jacking where water pressure exceeds that required to float the overlying ice. However, localized incision could occur, particularly at hydropotential barriers (e.g., Carter et al., 2015). Thus, the canal imaged by Horgan et al. (2013) crossing the grounding zone downstream of SLW may be a localized feature, possibly eroded by tidal currents or a relic from a time of greater subglacial hydrologic activity.

5. Conclusions

Although we cannot constrain the last time ice grounded over Subglacial Lake Whillans, the dynamic history of the lake combined with the lack of rainout debris from the actively melting ice above (Fisher et al., 2015), suggest the lacustrine history of the site is short, probably on the order of decades. This subglacial environment is analogous to a non-vegetated wetland within a terrestrial coastal plain, where water bodies tend to be broad and shallow due to the low topographic relief. In the subglacial equivalent, ice may frequently ground following hydrologic adjustments, limiting the long-term persistence of shallow lakes and their sediments. With weak topographic control, frequent avulsions make flow paths dynamic and difficult to predict (e.g., Carter et al., 2013). Consequently, ice stream subglacial lakes that occur in association with soft sedimentary beds, as on ice plains, are ephemeral features and poorly preserved in the geologic record, unlike lakes in deep bedrock depressions, such as subglacial lakes Vostok and Ellsworth, which hold greater potential for preserving undisturbed paleoenvironmental archives (Bentley et al., 2011; Filina et al., 2008; Siegert et al., 2001).

Lacustrine sediments beneath SLW were anticipated to provide a longer-term record of the dynamic hydrologic system under this portion of the Antarctic Ice Sheet. Instead we found that the lake was floored by till, which provided insight into the present environment beneath the ice stream, and specifically its ice plain. These regions are likely to have existed over many segments of the ice sheet grounding line during its history and influence both how ice sheets grow and their sensitivity to external climate forcing. Our results suggest that most subglacial sediment transport across the ice plain occurs through a shallow (cm's thick) layer of till with minimal sediment contribution from the subglacial hydrologic network. This low subglacial sediment flux to the Whillans' grounding zone is unlikely to stabilize the grounding zone position against either ocean thermal forcing or changes in ice dynamics and suggests that grounding zones could be more reactive to sea-level rise than previously thought.

Acknowledgements

This work was funded through the NSF (grants ANT-0839107, ANT-0839059, and PLR-1346260). Additional funding for instrumentation development and testing was provided by grants from NOAA (grants NA04OAR4600167 and NA05OAR4311117), Gordon and Betty Moore Foundation (grants 2339 and 2992), and the Alfred E. Alquist Seismic Safety Commission of California (contract SCC 2010-07).

We are grateful to the University of Nebraska-Lincoln drill team and WISSARD traverse personnel, Air National Guard and Kenn Borek Air for their technical and logistical support, without which this work would not have been possible. We also thank Julie Brigham-Grette for use of the UMass core processing facility, FSU-ARF for taking core x-radiographs, and Rebecca Puttkammer for her help in processing samples.

The manuscript was written by TOH and RDP; SAB conducted measurements of NRM and AMS; TOH described the micromorphology and lithology; and RDP, ST, and RPS contributed to the study design and acquisition of samples.

Appendix A. Sand mineralogy

Composition of the sand fraction at SLW is statistically indistinguishable from sediments recovered upstream (at UpB) and very similar to previously described samples from the Siple Coast and Eastern Ross Sea Region (Licht et al., 2005). In order of decreasing abundance, the 500–2000 μm size fraction contained quartz (37%), feldspar (24%), felsic intrusive lithic fragments (19%), metamorphic lithic fragments (14%), and intermediate intrusive lithic fragments (3%). Sedimentary lithic fragments, extrusive lithic fragments, heavy minerals and mafic intrusive lithic fragments each constitute $\leq$1% (Fig. S1). Felsic intrusive grains commonly display evidence of hydrothermal alteration, either by chlorite replacement of biotite or seritization of feldspars grains. Metamorphic grains are dominantly schists and phyllites, and sedimentary lithics include diamictites, mudstones, limestone, and dolomite.

Appendix B. Microfabrics

Microfabrics support this interpretation showing structures consistent with ductile shear and very little disturbance from degassing. Skel-insepic intergrading to skel-lattisepic plasmic fabrics and rotational microstructures are dominant in all of the sampled intervals. Large (0.1–0.5 mm wide) planar fractures are abundant in the shallowest piston core and percussion core thin sections. In the piston core sample, fractures display a polygonal pattern suggesting they formed by desiccation. Samples used in AMS and NRM were taken immediately after the cores were split and should not have been affected. In the percussion core sample, fractures are dominantly subhorizontal and may have formed from dilation and pressure release caused by the 'hammering' of the corer. Planar plasmic fabrics occur in proximity to the fractures where they are aligned parallel to the dominant fracture orientation. We interpret these fabrics as evidence of coring disturbance, which may overprint natural magnetic fabrics in the percussion core. Subvertical planar fabrics occur in the deepest piston core sample (see masepic fabric in Fig. S2). The corresponding AMS fabrics have an anomalous vertical trend interpreted as evidence of core stretching (see horizontal K_{min} vectors in Fig. 3a). Degassing tubules tend to be very fine ($<$0.1 mm wide), rare ($<$2% of area), and most importantly show very limited disturbance of the surrounding fabric suggesting that degassing has not significantly affected magnetic fabrics in the cores.

Appendix C. Magnetic granulometry

C.1. Methods

The hysteresis parameters saturation magnetization, saturation remanence, coercivity, coercivity of remanence, and high-field magnetic susceptibility (M_S, M_R, B_C, B_{CR}, and χ_{hf}, respectively), were measured on a Princeton Measurements Corp. Vibrating Sample Magnetometer (VSM) in a 1-T peak field. Measurements were made on bulk sediment to assess the average domain state responsible for the natural remanent magnetization and anisotropy of magnetic susceptibility behavior. Raw hysteresis data were processed by using χ_{HF} (calculated between 0.7 T and 1 T) to remove the paramagnetic contribution to the induced magnetization, and then normalized by mass. The hysteresis parameters saturation magnetization (M_S), saturation remanence (M_R) and coercivity (H_C) were determined from the paramagnetic-corrected data. The coercivity of remanence (H_{CR}) was determined through the DC-demagnetization of a saturation isothermal remanent magnetization imparted in a 1 T field. The S-ratio was measured by imparting a 1 T isothermal remanent magnetization, followed by the application of a 300 mT backfield, and calculating S as $M_{R(-300\text{-mT})}/M_{R(1\text{-T})}$.

Thermomagnetic curves were measured on an AGICO KLY-4 Kappabridge at Montclair State University. Magnetic susceptibility was measured on a sample size of 500–600 mg of dry sediment during heating and cooling from 20–700 °C in a flowing argon gas atmosphere. Raw data were corrected for the furnace contribution and normalized by mass.

Grain mounts were prepared to observe Fe-oxide mineral assemblages via electron microscopy following Darby and Bischof (1996). The 45–500 μm size fraction was wet sieved and then processed using a Franz magnetic separator. The magnetic fraction was examined under an Olympus SZ12 stereomicroscope. Grains with metallic luster were manually picked from the magnetic fraction, mounted in epoxy, polished, and carbon-coated. Polished specimens were examined using a Hitachi S-3400N Scanning Electron Microscope (SEM) equipped with a Bruker X-flash X-ray microanalysis system. Standardless quantitative analysis was performed using the Phi–Rho–Z standardless quantitative analysis routine in Bruker's Esprit 1.9.3 software. Tests of the Phi–Rho–Z routine on microprobe quality mineral standards yielded results within 0.05 to 1% relative of the published compositions for major elements (wt% $>$ 5%) and within 0.05–0.5% relative for minor elements ($<$5 wt%).

C.2. Results

The magnetic mineral assemblage in SLW-1 PC1 and PEC-1 is comprised of magnetite and minor amounts of ilmenite and hematite, with the latter likely occurring as nano-scale lamellae in (hemo)ilmenite. The magnetic mineral assemblage is uniform throughout PC1, consistent with relatively constant Fe/Ti ratios determined from XRF measurements (Fig. 2). Magnetic domain state was determined from the median destructive field of the NRM (MDF_{NRM}), the alternating field value at which 50% of the NRM is removed, and from hysteresis measurements. MDF_{NRM} values in PC1 are between 35 and 40 mT, consistent with fine PSD magnetite. Hysteresis parameters in bulk samples from SLW-1 piston core 1 (PC1) and percussion core 1 (PEC-1) are dominated by multidomain grains, with M_R/M_S values between 0.04 and 0.06 and B_{cr}/B_c values between 5 and 6 (Table S1; Fig. S4). This is consistent with lithic fragment abundances, for which felsic and intermediate intrusive fragments (i.e., coarse grained lithologies) are abundant, and extrusive fragments (fine grained lithologies) comprise $<$1% of the assemblage (Appendix A).

Magnetic mineralogy was determined from thermomagnetic curves, S-ratios, and energy-dispersive X-ray spectroscopy (EDX). S-ratios are nearly 1 for all samples (Table S1), indicative of low coercivity minerals such as magnetite. Susceptibility vs. temperature is invariant between 20 and 380 °C. Susceptibility increases between 380 and 450 °C, which is likely a thermochemical alteration feature. This is followed by rapid loss of signal between 565 °C and 610 °C, indicative of low-Ti titanomagnetite and magnetite that are slightly oxidized (Fig. S4). A continued loss of signal is observed between 600 and 700 °C, which is suggestive of hematite. This feature is reversible in the heating and cooling curves. As no hematite grains were observed in the SEM and the S-ratios are uniformly near 1, we infer this high-temperature signal as originating from nano-scale hematite intergrowths within ilmenite. SEM and EDX data support the thermomagnetic data. Observations of magnetic grains extracted from the 45–500 μm fraction reveal homogeneous magnetite (72% wt% Fe and no other detectable cations) and homogeneous ilmenite in which the Fe wt% (38%) is very slightly enriched above the stoichiometric value (36.8%).

Appendix D. Supplementary material

Supplementary material related to this article can be found online at http://dx.doi.org/10.1016/j.epsl.2016.03.036.

References

Alley, R.B., Anandakrishnan, S., Dupont, T.K., Parizek, B.R., Pollard, D., 2007. Effect of sedimentation on ice-sheet grounding-line stability. Science 315, 1838–1841. http://dx.doi.org/10.1126/science.1138396.

Anandakrishnan, S., Alley, R.B., 1997. Stagnation of ice stream C, West Antarctica by water piracy. Geophys. Res. Lett. 24, 265–268. http://dx.doi.org/10.1029/96GL04016.

Anandakrishnan, S., Blankenship, D.D., Alley, R.B., Stoffa, P.L., 1998. Influence of subglacial geology on the position of a West Antarctic ice stream from seismic observations. Nature 394, 62–65.

Anandakrishnan, S., Catania, G.A., Alley, R.B., Horgan, H.J., 2007. Discovery of till deposition at the grounding line of Whillans Ice Stream. Science 315, 1835–1838. http://dx.doi.org/10.1126/science.1138393.

Bamber, J.L., Riva, R.E.M., Vermeersen, B.L., LeBrocq, A.M., 2009. Reassessment of the potential sea-level rise from a collapse of the West Antarctic Ice Sheet. Science 324, 901–903. http://dx.doi.org/10.1126/science.1169335.

Bell, R.E., Studinger, M., Shuman, C.A., Fahnestock, M.A., Joughin, I., 2007. Large subglacial lakes in East Antarctica at the onset of fast-flowing ice streams. Nature 445, 904–907. http://dx.doi.org/10.1038/nature05554.

Benn, D., Evans, D.J., 2014. Glaciers and Glaciation. Routledge.

Bentley, M.J., Christoffersen, P., Hodgson, D.A., Smith, A.M., Tulaczyk, S., Le Brocq, A.M., 2011. Subglacial lake sediments and sedimentary processes: potential archives of ice sheet evolution, past environmental change, and the presence of life. In: Antarctic Subglacial Aquatic Environments, pp. 83–110.

Bindschadler, R.A., King, M.A., Alley, R.B., Anandakrishnan, S., Padman, L., 2003. Tidally controlled stick-slip discharge of a West Antarctic ice. Science 301, 1087–1089. http://dx.doi.org/10.1126/science.1087231.

Carter, S.P., Fricker, H.A., Siegfried, M.R., 2013. Evidence of rapid subglacial water piracy under Whillans Ice Stream, West Antarctica. J. Glaciol. 59, 1147–1162. http://dx.doi.org/10.3189/2013JoG13J085.

Carter, S.P., Fricker, H.A., Siegfried, M.R., 2015. Active lakes in Antarctica survive on a sedimentary substrate—Part 1: Theory. Cryosphere Discuss. 9, 2053–2099.

Christianson, K., Jacobel, R.W., Horgan, H.J., Anandakrishnan, S., Alley, R.B., 2012. Subglacial Lake Whillans — ice-penetrating radar and GPS observations of a shallow active reservoir beneath a West Antarctic ice stream. Earth Planet. Sci. Lett. 331–332, 237–245. http://dx.doi.org/10.1016/j.epsl.2012.03.013.

Christner, B.C., Priscu, J.C., Achberger, A.M., Barbante, C., Carter, S.P., Christianson, K., Michaud, A.B., Mikucki, J.A., Mitchell, A.C., Skidmore, M.L., Vick-Majors, T.J., Adkins, W.P., Anandakrishnan, S., Barcheck, G., Beem, L., Behar, A., Beitch, M., Bolsey, R., Branecky, C., Edwards, R., Fisher, A., Fricker, H.A., Foley, N., Guthrie, B., Hodson, T., Jacobel, R., Kelley, S., Mankoff, K.D., McBryan, E., Powell, R., Purcell, A., Sampson, D., Scherer, R., Sherve, J., Siegfried, M., Tulaczyk, S., 2014. A microbial ecosystem beneath the West Antarctic ice sheet. Nature 512, 310–313. http://dx.doi.org/10.1038/nature13667.

Clarke, G.K.C., 2005. Subglacial processes. Annu. Rev. Earth Planet. Sci. 33, 247–276. http://dx.doi.org/10.1146/annurev.earth.33.092203.122621.

Cowan, E.A., Christoffersen, P., Powell, R.D., Talarico, F.M., 2014. Dynamics of the late Plio-Pleistocene West Antarctic Ice Sheet documented in subglacial diamictites, AND-1B drill core. Glob. Planet. Change 119, 56–70. http://dx.doi.org/10.1016/j.gloplacha.2014.05.011.

Darby, D.A., Bischof, J.F., 1996. A statistical approach to source determination of lithic and Fe-oxide grains: an example from the Alpha Ridge, Arctic Ocean. J. Sedimentary Res. 66, 599–607.

Dowdeswell, J.A., Fugelli, E.M.G., 2012. The seismic architecture and geometry of grounding-zone wedges formed at the marine margins of past ice sheets. Geol. Soc. Am. Bull. 124, 1750–1761.

Eyles, N., Day, T.E., Gavican, A., 1987. Depositional controls on the magnetic characteristics of lodgement tills and other glacial diamict facies. Can. J. Earth Sci. 24, 2436–2458. http://dx.doi.org/10.1139/e87-229.

Filina, I.Y., Blankenship, D.D., Thoma, M., Lukin, V.V., Masolov, V.N., Sen, M.K., 2008. New 3D bathymetry and sediment distribution in Lake Vostok: implication for pre-glacial origin and numerical modeling of the internal processes within the lake. Earth Planet. Sci. Lett. 276, 106–114. http://dx.doi.org/10.1016/j.epsl.2008.09.012.

Fisher, A.T., Mankoff, K.D., Tulaczyk, S.M., Tyler, S.W., Foley, N., Team, W.S., 2015. High geothermal heat flux measured below the West Antarctic Ice Sheet. Nat. Adv., 1–9.

Fricker, H.A., Scambos, T., 2009. Connected subglacial lake activity on lower Mercer and Whillans Ice Streams, West Antarctica, 2003–2008. J. Glaciol. 55, 303–315. http://dx.doi.org/10.3189/002214309788608813.

Fricker, H.A., Scambos, T., Bindschadler, R., Padman, L., 2007. An active subglacial water system in West Antarctica mapped from space. Science 315, 1544–1548. http://dx.doi.org/10.1126/science.1136897.

Gravenor, C.P., Stupavsky, M., Symons, D.T.A., 1973. Paleomagnetism and its relationship to till deposition. Can. J. Earth Sci. http://dx.doi.org/10.1139/e73-092.

Hiemstra, J.F., Rijsdijk, K.F., 2003. Observing artificially induced strain: implications for subglacial deformation. J. Quat. Sci. 18, 373–383. http://dx.doi.org/10.1002/jqs.769.

Hodgson, D.A., Bentley, M.J., Smith, A., Klepacki, J., Makinson, K., Smith, M., Saw, K., Scherer, R., Powell, R., Tulaczyk, S., Rose, M., Pearce, D., Mowlem, M., Keen, P., Siegert, M.J., Hodgson, D.A., 2016. Technologies for retrieving sediment cores in Antarctic subglacial settings. Philos. Trans. R. Soc. A, Math. Phys. Eng. Sci. 374. http://dx.doi.org/10.1098/rsta.2015.0056.

Hooyer, T.S., Iverson, N.R., Lagroix, F., Thomason, J.F., 2008. Magnetic fabric of sheared till: a strain indicator for evaluating the bed deformation model of glacier flow. J. Geophys. Res. 113, F02002. http://dx.doi.org/10.1029/2007JF000757.

Horgan, H.J., Alley, R.B., Christianson, K., Jacobel, R.W., Anandakrishnan, S., Muto, A., Beem, L.H., Siegfried, M.R., 2013. Estuaries beneath ice sheets. Geology 41, 1159–1162. http://dx.doi.org/10.1130/G34654.1.

Horgan, H.J., Anandakrishnan, S., Jacobel, R.W., Christianson, K., Alley, R.B., Heeszel, D.S., Picotti, S., Walter, J.I., 2012. Subglacial Lake Whillans — seismic observations of a shallow active reservoir beneath a West Antarctic ice stream. Earth Planet. Sci. Lett. 331–332, 201–209. http://dx.doi.org/10.1016/j.epsl.2012.02.023.

IPCC, 2014. Climate Change 2014: Impacts, Adaptation, and Vulnerability. Part A: Global and Sectoral Aspects. Cambridge University Press, Cambridge, United Kingdom and New York, NY, USA.

Iverson, N.R., Hooyer, T.S., Thomason, J.F., Graesch, M., Shumway, J.R., 2008. The experimental basis for interpreting particle and magnetic fabrics of sheared till. Earth Surf. Process. Landf. 33, 627–645. http://dx.doi.org/10.1002/esp.1666.

Joughin, I., Smith, B.E., Medley, B., 2014. Marine ice sheet collapse potentially under way for the Thwaites Glacier Basin, West Antarctica. Science 344, 735–738. http://dx.doi.org/10.1126/science.1249055.

Khatwa, A., Tulaczyk, S., 2001. Microstructural interpretations of modern and Pleistocene subglacially deformed sediments: the relative role of parent material and subglacial processes. J. Quat. Sci. 16, 507–517. http://dx.doi.org/10.1002/jqs.609.

Licht, K.J., Lederer, J.R., Jeffrey Swope, R., 2005. Provenance of LGM glacial till (sand fraction) across the Ross embayment, Antarctica. Quat. Sci. Rev. 24, 1499–1520. http://dx.doi.org/10.1016/j.quascirev.2004.10.017.

Munro-Stasiuk, M.J., 2003. Subglacial Lake McGregor, south-central Alberta, Canada. Sediment. Geol. 160, 325–350. http://dx.doi.org/10.1016/S0037-0738(03)00090-3.

Priscu, J.C., Adams, E.E., Lyons, W.B., Voytek, M.A., Mogk, D.W., Brown, R.L., McKay, C.P., Takacs, C.D., Welch, K.A., Wolf, C.F., Kirshtein, J.D., Avci, R., 1999. Geomicrobiology of subglacial ice above Lake Vostok, Antarctica. Science 286, 2141–2144. http://dx.doi.org/10.1126/science.286.5447.2141.

Pritchard, H.D., Ligtenberg, S.R.M., Fricker, H.A., Vaughan, D.G., van den Broeke, M.R., Padman, L., 2012. Antarctic ice-sheet loss driven by basal melting of ice shelves. Nature 484, 502–505. http://dx.doi.org/10.1038/nature10968.

Rignot, E., Jacobs, S.S., 2002. Rapid bottom melting widespread near Antarctic Ice Sheet grounding lines. Science 296, 2020–2023. http://dx.doi.org/10.1126/science.1070942.

Rignot, E., Mouginot, J., Morlighem, M., Seroussi, H., Scheuchl, B., 2014. Widespread, rapid grounding line retreat of Pine Island, Thwaites, Smith, and Kohler glaciers, West Antarctica, from 1992 to 2011. Geophys. Res. Lett. 41, 3502–3509. http://dx.doi.org/10.1002/2014GL060140.

Schoof, C., 2007. Marine ice-sheet dynamics. Part 1. The case of rapid sliding. J. Fluid Mech. 573, 27. http://dx.doi.org/10.1017/S0022112006003570.

Siegert, M.J., Ellis-Evans, J.C., Tranter, M., Mayer, C., Petit, J.R., Salamatin, A., Priscu, J.C., 2001. Physical, chemical and biological processes in Lake Vostok and other Antarctic subglacial lakes. Nature 414, 603–609. http://dx.doi.org/10.1038/414603a.

Siegfried, M.R., Fricker, H.A., Roberts, M., Scambos, T.A., Tulaczyk, S., 2014. A decade of West Antarctic subglacial lake interactions from combined ICESat and CryoSat-2 altimetry. Geophys. Res. Lett. 41, 891–898. http://dx.doi.org/10.1002/2013GL058616.

Snowball, I., Mellström, A., Ahlstrand, E., Haltia, E., Nilsson, A., Ning, W., Muscheler, R., Brauer, A., 2013. An estimate of post-depositional remanent magnetization lock-in depth in organic rich varved lake sediments. Glob. Planet. Change 110, 264–277. http://dx.doi.org/10.1016/j.gloplacha.2013.10.005.

Stearns, L.A., Smith, B.E., Hamilton, G.S., 2008. Increased flow speed on a large East Antarctic outlet glacier caused by subglacial floods. Nat. Geosci. 1, 827–831. http://dx.doi.org/10.1038/ngeo356.

Stoner, J.S., Channell, J.E.T., Mazaud, A., Strano, S.E., Xuan, C., 2013. The influence of high-latitude flux lobes on the Holocene paleomagnetic record of IODP Site U1305 and the northern North Atlantic. Geochem. Geophys. Geosyst. 14, 4623–4646. http://dx.doi.org/10.1002/ggge.20272.

Stupavsky, M., Gravenor, C.P., Symons, D.T.A., 1974. Paleomagnetism and magnetic fabric of the Leaside and Sunnybrook Tills near Toronto, Ontario. Bull. Geol. Soc. Am. 85, 1233–1236. http://dx.doi.org/10.1130/0016-7606(1974)85<1233:PAMFOT>2.0.CO;2.

Tarling, D., Hrouda, F., 1993. The Magnetic Anisotropy of Rocks. Chapman and Hall, London.

Thouveny, N., Moreno, E., Delanghe, D., Candon, L., Lancelot, Y., Shackleton, N.J., 2000. Rock magnetic detection of distal ice-rafted debries: clue for the identification of Heinrich layers on the Portuguese margin. Earth Planet. Sci. Lett. 180, 61–75. http://dx.doi.org/10.1016/S0012-821X(00)00155-2.

Tulaczyk, S., Kamb, B., Scherer, R.P., Engelhardt, H.F., 1998. Sedimentary processes at the base of a West Antarctic ice stream: constraints from textural and compositional properties of subglacial debris. J. Sediment. Res. 68, 487–496.

Tulaczyk, S., Kamb, B., Engelhardt, H.F., 2000. Basal mechanics of Ice Stream B, West Antarctica: 1. Till mechanics. J. Geophys. Res., Solid Earth 105, 463–481.

Tulaczyk, S., Kamb, B., Engelhardt, H.F., 2001a. Estimates of effective stress beneath a modern West Antarctic ice stream from till preconsolidation and void ratio. Boreas 30, 101–114. http://dx.doi.org/10.1080/03009480175020313 4.

Tulaczyk, S.M., Scherer, R.P., Clark, C.D., 2001b. A ploughing model for the origin of weak tills beneath ice streams: a qualitative treatment. Quat. Int. 86, 59–70. http://dx.doi.org/10.1016/S1040-6182(01)00050-7.

Tulaczyk, S., Mikucki, J.A., Siegfried, M.R., Priscu, J.C., Barcheck, C.G., Beem, L.H., Behar, A., Burnett, J., Christner, B.C., Fisher, A.T., Fricker, H.A., Mankoff, K.D., Powell, R.D., Rack, F., Sampson, D., Scherer, R.P., Schwartz, S.Y., 2014. WISSARD at Subglacial Lake Whillans, West Antarctica: scientific operations and initial observations. Ann. Glaciol. 55, 51–58. http://dx.doi.org/10.3189/2014AoG65A009.

van der Meer, J.J., 1993. Microscopic evidence of subglacial deformation. Quat. Sci. Rev. 12, 553–587.

van der Meer, J.J.M., Menzies, J., 2011. The micromorphology of unconsolidated sediments. Sediment. Geol. 238, 213–232. http://dx.doi.org/10.1016/j.sedgeo.2011.04.013.

Weertman, J., 1974. Stability of the junction of an ice sheet and an ice shelf. J. Glaciol. 13, 3–11.

Wright, A., Siegert, M., 2012. A fourth inventory of Antarctic subglacial lakes. Antarct. Sci. 24, 1–6. http://dx.doi.org/10.1017/S095410201200048X.